Full Length Article

Towards high performance flexible planar supercapacitors: In-situ laser scribing doping and reduction of graphene oxide films

Aya Hamed [a,b,*], Amr Hessein [c,d], Ahmed Abd El-Moneim [a,d,e]

[a] Department of Materials Science and Engineering, Egypt-Japan University of Science and Technology, New Borg El Arab City, Alexandria 21934, Egypt
[b] Department of Mathematical and Physical Engineering, Faculty of Engineering, Alexandria University, Alexandria 21544, Egypt
[c] Department of Mathematical and Physical Engineering, Faculty of Engineering (Shoubra), Benha University, Cairo 11614, Egypt
[d] Graphene Center of Excellence for Energy and Electronic Applications, Egypt-Japan University of Science and Technology, Alexandria 21934, Egypt
[e] Basic and Applied Sciences Institute, Egypt-Japan University of Science and Technology, New Borg El Arab, Alexandria 21934, Egypt

ARTICLE INFO

ABSTRACT

A novel, scalable, single-step and low-synthesis temperature fabrication approach is proposed for real-time doping, reduction, and patterning of graphene oxide-based films supported on flexible polyethylene terephthalate (PET) substrate using a CO2 Laser system. Laser reduced graphene oxide (LrGO), nitrogen-doped laser reduced graphene oxide (N-LrGO), and sulfur-nitrogen co-doped laser reduced graphene oxide (SN-LrGO) planar supercapacitors (PSCs) are readily fabricated with the proposed approach. Structural and elemental characterizations prove the successful integration of nitrogen and sulfur atoms into the graphene framework with high contents up to 3.71 at% N and 1.82 at% S, and at a low density of structural defects. An areal capacitance as high as 13.8 mF cm^{-2} at 10 mV s^{-1} and a maximum power density of 151.7 mW cm^{-3} at an energy density of 0.152 mWh cm^{-3} is achieved by SN-LrGO PSC composed of 10 interdigitated fingers with an excellent retention rate after 2000 charging/discharging cycles at 0.125 mA cm^{-2}. Furthermore, higher operating voltage window and current ratings are easily achieved via series and parallel combinations of SN-LrGO PSCs directly on the same substrate. This manifests the versatility of the proposed approach for producing flexible and high-performance graphene-based electrochemical storage devices.

1. Introduction

With the increasing demand on portable and wearable integrated-electronics, there has been a growing interest in flexible, high-power, and large-capacity energy-storage systems. The potential usage of conventional charge storage devices such as batteries in these types of applications is currently limited due to their low-power capabilities, low charge/discharge rates, and short cycle-life. Planar supercapacitors (PSCs) are promising storage devices that have drawn great attention because of their high charge/discharge rate, long-life cycle, low maintenance, and outstanding power density [1,2]. Supercapacitors have several applications in wearable and implantable electronics, portable integrated on-chip and electronic devices, memory protection, battery enhancement, portable energy sources, and military and aerospace applications [1-4].

Unlike the conventional sandwich-structured supercapacitors, PSC is a kind of stand-alone power source recently received enormous attention as a complementary unit or even a replacement for micro-batteries. Typically, PSC incorporates interdigitated thin-film electrodes stacked with each other and finger current collectors, while a solid or a semi-solid electrolyte is layered on the surfaces and in the interspaces of the electrode. Basically, electrode material plays a decisive role in the performance of the PSCs. Various materials have been explored as electrode material for interdigitated planar SCs including metals oxides/hydroxides Such as MnO_2, $NiFe_2O_4$, and $Cu(OH)_2$ [5-7] carbonaceous materials such as CNFs and CNTs [8,9], conducting polymers such as PEDOT:PSS and polyaniline [10,11], and MXenes [12]. Hybrid electrode materials were also developed for interdigitated PSCs. For instance, L. Li et.al fabricated a highly-stretchable planar-SC from a hybrid multi-walled carbon nanotubes/polyaniline (MWCNTs/PANI) electrodes that attained a large areal capacitance of 44.13 mF cm^{-2} and yielded a power density of 0.07 mW cm^{-2} at an energy density of 0.004 mWh cm^{-2} [13].

---

* Corresponding author at: Department of Materials Science and Engineering, Egypt-Japan University of Science and Technology, New Borg El Arab City, Alexandria 21934, Egypt.
E-mail address: aya.kadi@ejust.edu.eg (A. Hamed).

Recently, Graphene has been extensively investigated as an electrode material due to its fascinating properties including high electrical and thermal conductivities, excellent mechanical strength, and high specific surface area [2,14,15]. Graphene is a two-dimensional carbon sheet that can be synthesized using different methods such as chemical vapor deposition (CVD), epitaxial growth, liquid-phase exfoliation, and electrochemical exfoliation [16-18]. However, these methods are known to be of low productivity that are not adequate for the mass production of electrical and electrochemical applications. Currently, large-scale production of graphene is achievable through the reduction of graphene oxide (GO) either by chemical or thermal methods [16,19]. Unfortunately, due to incomplete reduction or numerous structural defects, the quality of the produced graphene is far inferior compared to its counterparts from pristine graphene and physically grown graphene [18,20,21].

Alternatively, and due to the high-energy–density of its focused beam, the laser-based reduction is a versatile technique employed successfully to effectively reduce GO without the use of a reducing chemical agent and even without the need for high-temperature post-treatment. In the past decade, laser reduction of GO is extensively studied and the reduction mechanism was attributed to both the photochemical and the photothermal effects [22-26]. Laser reduced GO (LrGO) was first introduced in 2010 by Y. Zhang and his coworkers using femtosecond laser [27,28]. A breakthrough in laser reduction of GO was made by El-Kady et al. [29,30] who employed commercial LightScribe DVD drive for in-situ producing and patterning LrGO films via laser direct writing on GO/PET flexible substrate. With prolonged reduction time reached 20 min and multiple laser reduction cycles, El-Kady increased the electric conductivity of the LrGO films up to 1738 S m^{-1} and used these films for fabricating interdigitated PSC devices those achieve a 2.32 mF cm^{-2} areal specific capacitance at 16.8 mA cm^{-3}. Later, Guo et al. significantly reduced resistivity of LrGO flexible electronic applications to be equals to 3.91×10^{-5} Ω m by modulating the oxygen contents in the reduced GO region via optimizing the power of the 780 nm femtosecond laser [25]. However, till now, the performances and rate-capabilities of the LrGO-based PSCs still lack behind its counterparts PSCs fabricated from different materials or even hybrid-rGO fabricated and patterned with the other fabrication methods [31].

Currently, it is well accepted that the incorporation of heteroatoms in the graphene framework is able to modify its chemical and electronic properties [32,33]. The incorporation of heteroatoms dopant modulates the electrical conductivity, surface properties, chemical reactivity, and mechanical properties of graphene, which are prerequisites for high-performance energy storage applications [15,34]. Although the outstanding enhancements in the performance achieved for the conventional SCs upon graphene doping, this region of research still not fully explored for laser processed interdigitated PSC devices. One of the first attempts was conducted by Z. Peng and his co-workers in 2015 for the fabrication of interdigitated PSC from boron-doped laser-induced graphene LIG (B-LIG) [35]. In their work, the B-doping is achieved by coating a condensed layer of boric acid on the polyamide (PI) substrate prior to subjecting the substrate to commercial CO$_2$ laser writes. Although the novelty of the technique and the high attained areal capacitance of 16.5 mF cm^{-2} (three times higher than non-doped device), however, the complexity of the fabrication process may hinder the potential of this technique for mass production and practical applications. Later in 2017 and in an attempt to simplify the fabrication process, A. Lamberti et al. achieved self-doping of LIG films on polyimide with nitrogen for planar-SC applications through modulating the 10.6 μm CO$_2$ pulsed laser parameter, such as pulse frequency and scan speed [36]. However, the performance improvements of this method are limited by the very-low nitrogen doping level (<2.5 at%) resulted in the inferior electrochemical capacitance of the devices (~268 μF cm^{-2}).

In this regard, we present here a scalable low-cost, fast processing, and low-temperature novel technique for simultaneous doping, reduction, and patterning of GO films supported on flexible polyethylene terephthalate (PET) substrate for interdigitated PSC applications. Laser reduced graphene oxide (LrGO), nitrogen-doped LrGO (N-LrGO), and sulfur-nitrogen co-doped LrGO (SN-LrGO) films are successfully synthesized using laser scribing technique and single doping precursor. Thanks to the enormous number of defected sites evolved during the laser reduction process, also, the synergy between the S and N, higher doping levels (3.71 at% N, and 1.82 at% S) are easily realized. As a result, the produced doped films are found to depict higher electrical conductivity of 51 Sm^{-1} and 176 Sm^{-1} for N-LrGO, and SN-LrGO, respectively, much overcoming the 28 Sm^{-1} measured for the undoped LrGO film. Interdigitated PSCs were successfully fabricated using the doped electrodes and tested by means of cyclic voltammetry (CV), galvanic constant current charge–discharge (GCCD), and electrochemical impedance spectroscopy (EIS) measurements. The PSC fabricated from SN-LrGO recorded an approximately ten-fold increase in capacitance compared to PSC from pristine LrGO, where, the capacitance increased significantly from 1.15 mF cm^{-2} for LrGO to 11.35 mF cm^{-2} in the case of SN-LrGO at a current density of 0.125 mA cm^{-2}. All fabricated films also showed superior durability and mechanical flexibility such that the electric conductivity and the capacitance maintained their initial values after multiple bending and charging/discharging cycles. Furthermore, the impacts of increasing the number of interdigitated electrodes per substrate on the device performance as well as the series and parallel connection of multiple devices are also studied and found to be far practical. Hence, the proposed technique is proved to be a simple yet effective method to productively incorporate S and N atoms into graphene sheets with minimum defect density at low synthesis temperature for future on-chip flexible electronics.

2. Experimental

2.1. Materials

Graphite powder with 5–20 μm grain size is purchased from Fisher Scientific, UK. Urea [CH$_4$N$_2$O, greater than99%] and thiourea [CH$_4$N$_2$S, greater than99%] are obtained from Sigma Aldrich, Germany. Phosphoric acid (H$_3$PO$_4$) and polyvinyl alcohol (PVA, average Mw = 85000 g/mol) are purchased from Sigma Aldrich, Germany. All other chemicals are reagent grade and used as received without any additional purification. Polyethylene Terephthalate (PET) substrates with 100 μm thickness are commercially sourced.

2.2. Preparation of GO, N-GO, and SN-GO films supported on PET substrate

Graphite oxide was synthesized from graphite using the modified Hummer's method [37,38]. The prepared Graphite oxide was dispersed in distilled water with an initial concentration of 3 mg ml^{-1} by magnetic stirring. The graphite oxide dispersion is exfoliated into graphene oxide (GO) through ultrasonication for 1 hr using an ultrasonic bath which is followed by a mild ultrasonication for 2 hrs in an ice bath using a probe sonication. The doping process was performed by adding 20 wt% of urea in the case of N-doping and 20 wt% thiourea in the case of SN-doping to the graphene oxide solution right after bath ultrasonication and before the probe sonication step. The obtained GO-based solutions were centrifuged at 3000 rpm for 20 min to remove the non-exfoliated graphite oxide particles. Flexible PET substrates with dimensions 10 cm × 10 cm, were first cleaned for 20 min by ultrasonication in ethanol and then rinsed with water. After drying at room temperature, the cleaned substrates were subjected to oxygen plasma treatment at 75 W for 10 min in order to enhance the adhesion of GO to the substrate. All GO-based solutions were drop-casted onto the pre-cleaned PET substrates then they were left to dry naturally at ambient conditions.

2.3. Fabrication of LrGO, N-LrGO, and SN-LrGO electrodes

The simultaneous laser reduction, doping, and electrode patterning of the dried GO films are achieved in one step by using a high-powered 10.6 μm CO_2 commercial laser engraving machine (Versa LASER, VLS 3.50) [26,39]. The optimized laser parameters used for our films processing are 3.5 W for power, and 18% of maximum laser speed using the standard 2-inch lens. The ultrasonication effect together with the localized heating induced by laser reduction leads to nitrogen and sulfur/nitrogen to be incorporated into the reduced graphene oxide lattice structure this will be further explained in the materials forming mechanism. A detailed illustration of the fabrication process of the electrodes is schematically depicted in Fig. 1(a).

2.4. Assembly of planar interdigitated supercapacitors

A PSC design having six interdigitated fingers is shown in Fig. 1(b). The gap between the fingers of the interdigitated electrode was kept constant, 1 mm; which is the maximum resolution that was obtained using our CO_2 laser system. The width of the fingers was varied, from 6.75 to 2.1, to bring electrodes with 4, 6, 8, and 10 interdigitated fingers as shown in supplementary information Fig. S5. Copper tape was applied to the common area of the interdigitated electrodes to make better contact with the potentiostat terminals then it was covered with Kapton tape to prevent short circuit. Finally, a layer of gel electrolyte was painted on the device and is left for 4 – 6 hrs. to completely wet the interdigitated electrodes. To prepare the gel electrolyte, 1 gm of poly vinyl alcohol (PVA) was dissolved in 10 ml of distilled water with vigorous stirring and heating to 85 °C until a clear solution is obtained. After it cools down, 0.09 mol of phosphoric acid (H_3PO_4) was added to the solution and stirred to form the gel electrolyte [40]. The whole PSC cell was wrapped using Kapton tape and became ready for electrochemical measurements.

2.5. Material characterization

The morphology of LrGO-based films was determined using Scanning Electron Microscopy "SEM" (JEOL JSM-6010LV), and Transmission Electron Microscopy "TEM" (JEOL JEM-2010F). LrGO sheets were re-suspended in pure ethanol and the suspension was drop-casted on the copper grid for TEM measurements. To explore the structural properties and bonding configurations of the LrGO-based films; XRD, FT-IR, XPS and Raman spectroscopy measurement techniques were conducted. The XRD was performed with (Shimadzu, XRD-6100). The Raman scattering spectroscopy was measured with (Bruker, Senterra II) Raman microscope unit at an excitation wavelength λ_L = of 532 nm. The FTIR spectra were measured with (Bruker, VERTEX 70v) Spectrometer equipped with an ATR unit. XPS was collected on K-ALPHA (ThermoFisher Scientific, USA) with monochromatic X-ray Al K-alpha radiation −10 to 1350 eV and spot size 400 μm at pressure 10^{-9} mbar with full-spectrum pass energy 200 eV and at narrow-spectrum 50 eV.

The electrical conductivity σ (Sm^{-1}) of the films was measured employing a two-probe configuration using Keithley 2400 source meter unit and calculated from:

$$\sigma = \frac{L}{RA_t} \tag{1}$$

where; L (m) is the length of the film, R (Ω) is the resistance of the film equals to the inverse of the slope of IV curve and A_t (m^2) is the cross-sectional area of the film which equals to width of the film multiplied by its thickness. A bending test rig was home built to test change in conductivity at different bending angles and bending cycles. The test rig is presented in supplementary information Fig. S2.

2.6. Electrochemical measurements

The electrochemical performances of the assembled supercapacitor devices were assessed using cyclic voltammetry (CV), galvanostatic charge–discharge (GCD), in addition to electrochemical impedance spectroscopy (EIS) electrochemical characterization tools using Versa-STAT4 potentiostat. The CV behavior of the electrodes was studied within a potential window of (0–1) V at scan rates of (10–100) mV s^{-1}. GCD measurements were carried out at constant current in the range of (0.029–0.2) mA cm^{-2}. The volumetric C_v (F cm^{-3}) and areal C_a (F cm^{-2}) specific capacitances, the Energy density E (Wh cm^{-3}) and the power density P (W cm^{-3}) of the tested PSC devices were calculated from GCD and EIS analysis results as reported in details in [41,42]. The effective area (including those of electrode fingers and gap between fingers) of
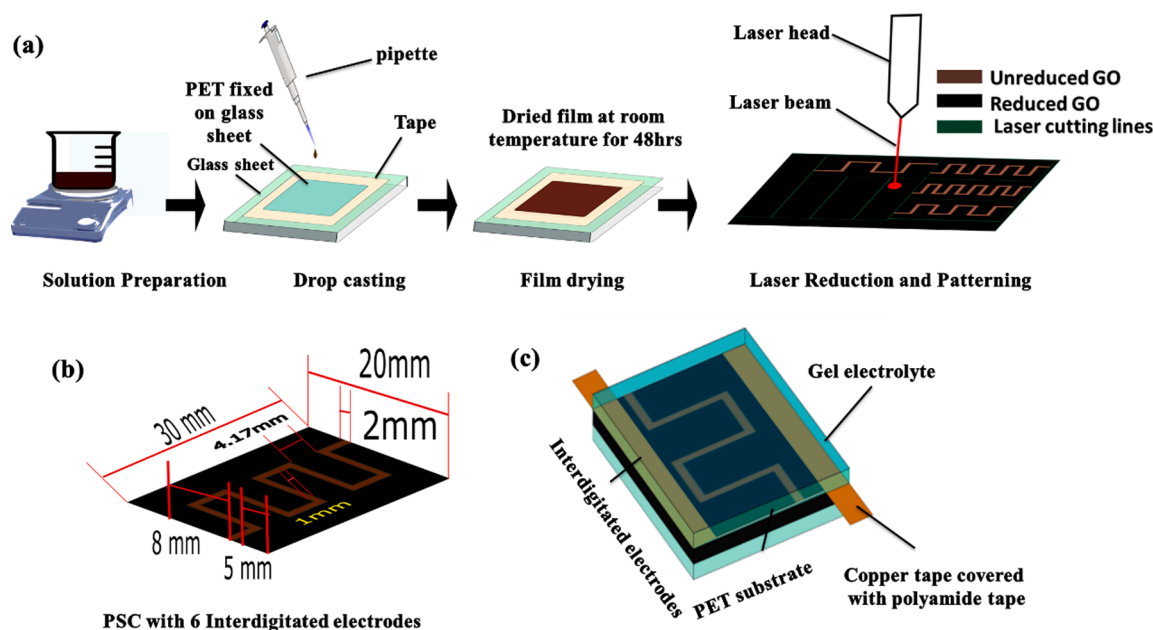

Fig. 1. Schematic illustration shows the steps of the fabrication process of the electrode: drop-casting, laser reduction, and patterning process (a), the dimensions of the interdigitated electrode with four fingers (b), assembly of supercapacitor interdigitated PSC cell (c).

the PSCs was determined as 2.4 cm^2, whereas the thicknesses of the active regions, measured using a confocal laser microscope, are approximately equal to 76, 64 and 63 μm for LrGO, N-LrGO and SN-LrGO electrodes, respectively.

3. Results and discussions

3.1. Morphology of LrGO-based films

The surface morphology of the fabricated films was examined by SEM, Fig. 2(a–d). The image of pristine LrGO film, Fig. 2(a), shows typical mud-cracked like structure that result from the release of gaseous product by the deoxygenation of the GO film with photothermal reduction process [26]. Closer inspection, Fig. 2(b), shows that the film is made up of unordered 3D stacking of overlapped rGO nanoflakes. No change in the surface morphology of LrGO film was observed with N-doping and SN-co-doping, Fig. 2(c) and (d). In fact, the 3D structure and porous morphology is important for providing more accessible surface area for ion diffusion and hence better capacitive performance. To demonstrate the reliability of the proposed technique and the laser reducing effect, the cross-sections of the films were measured using SEM. The results are shown in the supplementary information, Fig. S1. Thicknesses obtained from SEM measurements were comparable to those measured using confocal laser microscope. The figures show that the thicknesses of the films were fully reduced by means of the laser scribing technique. Doped films showed lower thickness compared to pristine LrGO. This may be due to difference in thermal responses and thermal conductivities of the three materials towards laser localized heating effect [43]. The reduced thickness necessarily enhances supercapacitor gravimetric figures for example: gravimetric capacitance, energy, and power densities.

The 3D structure of the fabricated films was further characterized using TEM images, Fig. 2(e–h). The images disclosed a laminar morphology for all films. A significant reduction in surface corrugation, folding, of GO, Fig. 2(e), was noticed after laser reduction, Fig. 2(f). This is because most of the oxygen groups have been removed thus releasing some strain. Meanwhile, both N-LrGO and SN-LrGO films, Fig. 2(h) showed more surface corrugation compared to prisitne LrGO film, though more folding is observed in the SN-LrGO nanotructure, Fig. 2(h). This is due to the introduction of heteroatom, nitrogen atom and nitrogen-sulfur atoms into the graphitic structure which results in induced stresses upon exfoliation in the presence of foreign atoms. Due to the difference in the atomic size of S compared to C and N, the insertion of S into the plane of graphitic carbon is harder than N, and hence induces more stresses. It can, therefore, be said that doping with heteroatoms, particulary with SN-co-doping, generally disrupts the planar structure of the graphene sheets.

3.2. Structural and compositional characterization of LrGO-based films

Fig. 3(a) shows the XRD patterns of GO, LrGO, N-LrGO, and SN-LrGO films. The pattern for GO is distinguished by a sharp peak at 9.7°, that correspond to the diffraction from the (0 0 1) plane. The patterns acquired by the LrGO, N-LrGO and SN-LrGO reveal the disappearance of the sharp (0 0 1) peak of GO along with an appearance of a single broad-peak located at 23.7°, 25.6° and 25.7°, respectively, assigned for the (0 0 2) plane typical characteristic of rGO. Using Bragg's equation, the value of interlayer spacing (d) for GO is significantly reduced from 0.91 nm to 0.375, 0.348 and 0.346 nm for LrGO, N-LrGO, and SN-LrGO, respectively. These changes indicate the recovery of the graphitic structure after successful removal of oxygen-functionalities from GO with laser treatment [44,45]. Meanwhile, the slightly lower d values for the N-LrGO and the SN-LrGO compared to the LrGO suggests the assisted-reduction role of the urea and thiourea for further reducing the GO [46].

The FTIR spectra collected from GO, LrGO, N-LrGO, and SN-LrGO films are shown in Fig. 3(b). The spectrum for the GO film is well indexed with the vibrational modes of the oxygen and hydrogen containing functional groups commonly attained by the GO [47]. After the laser treatment, the absorption bands related to the hydroxyl —OH (3448 cm^{-1}, 2960 cm^{-1} and 1420 cm^{-1}), the carboxyl and the carbonyl C=O (1734 cm^{-1}), the epoxide C—O (1230 cm^{-1}), and the alkoxy C—O—C (1042 cm^{-1}) in GO are significantly reduced in the spectra of all examined films [26]. Meanwhile, a major peak related to the C=C stretching mode in the aromatic regions of carbon network is observed in all recorded spectra at 1615 cm^{-1}. This peak becomes more prominent with doping, confirming an efficient restoration of sp^2-domains (π-π conjugation) of the graphitic structure. On the other hand, the spectra for the N-LrGO, and SN-LrGO films show minor absorption bands at 1580 and 1151 cm^{-1} assigned to the stretching vibration modes of the C=N bonds in the basal plane, and the C—N bonds in the secondary amides, respectively [48,49]. The spectrum for SN-doped film shows absorption bands at 772 and 604 cm^{-1}, typical of the thiophene—S (C—S—C) bond vibration and a band at 490 cm^{-1} typical of sulfoxide form (SO$_X$) [50]. No peaks related to direct bonding between N and S are detected in the spectrum of SN-LrGO film. These observations demonstrate that the N and S atoms are doped with different covalent bonding configurations in the rGO sheets.

The acquired Raman spectra from the LrGO, N-LrGO, and SN-LrGO films are shown in Fig. 3(c), where they display the characteristic
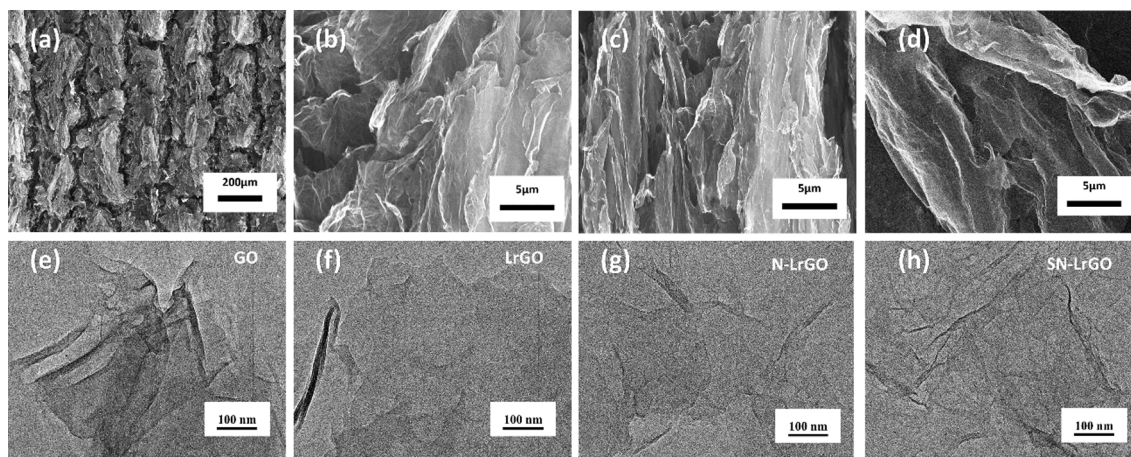

Fig. 2. SEM images of; LrGO film at low (a) and high (b) magnifications, and N-LrGO (c) and SN-LrGO (d) films at high magnification. High resolution TEM images of GO (e), LrGO (f), N-LrGO (g) and SN-LrGO (h) films.
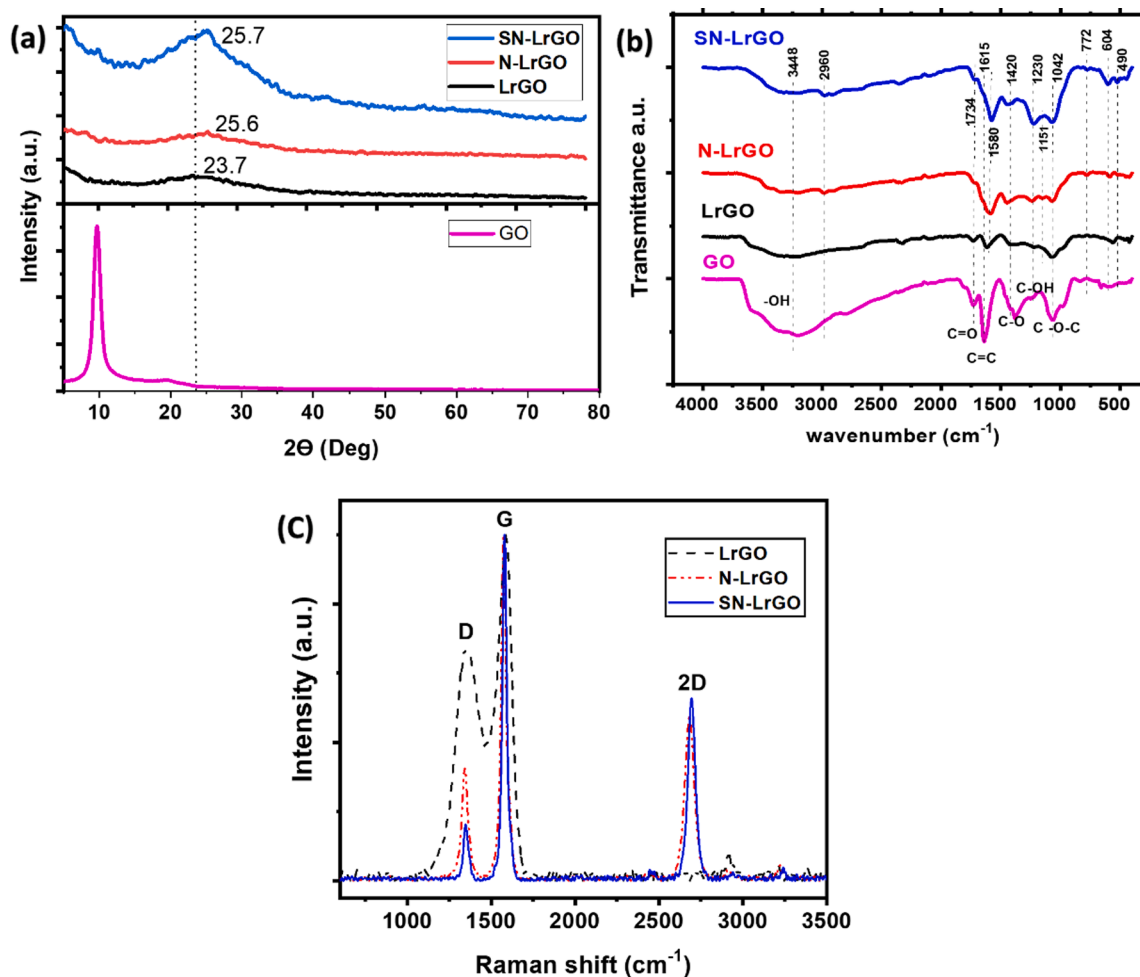
Fig. 3. XRD patterns (a), FTIR (b) and Raman spectra (c) for GO, LrGO, N-LrGO, and SN-LrGO films.

disordered D-band, ordered G-band and 2D-band at around 1350, 1585, and 2690 cm^{-1} for graphitic structures [51-54]. A down shift in the peak position and variation in intensity of the 2D band are observed by doping. The I_{2D}/I_G value gives perceptiveness about conversion of sp^3 carbon (which is a characteristic for unreduced GO) into sp^2 carbon (that is indicative for graphitization) and number of exfoliated graphene layers, as well [55]. I_{2D}/I_G for LrGO, N-LrGO and SN-LrGO films achieved values of 0.018, 0.82 and 0.87, respectively, revealing the transfer of the pristine LrGO film from multilayer to few-layered structure by doping, particularly with SN-doping. While, the I_D/I_G value is used to look into the nature and quantity of defects in the rGO sheets via defining the following terms; the average distance between defects (L^2_D), defect density per cm^2 (η_D) and crystallite size (Lsp^2) as per equations (2–4) [54,56–58]. Noticeably, the G band for the doped and co-doped samples undergoes a decrease in linewidth, which is commonly interpreted as a result of doping. Doping shifts fermi level away from the Dirac point, decreasing the probability of excited charge carrier recombination. The reduced recombination sharpens the G peak and decreases its FWHM. [59,60].

$$\eta_D = \frac{2.4 \times 10^{22}}{\lambda_L^4} \frac{I_D}{I_G} \qquad (2)$$

$$L_D^2\left(nm^2\right) = \left(2.4 \times 10^{-9}\right)\lambda_L^4 \left(\frac{I_D}{I_G}\right)^{-1}, \qquad (3)$$

$$L_{sp^2} = \frac{560}{E_L^4}\frac{I_G}{I_D} = \left(2.4 \times 10^{-10}\right)\lambda_L^4 \left(\frac{I_D}{I_G}\right)^{-1} \qquad (4)$$

A closer inspection of the results in **Table S1** reveals significant drop in η_D along with a remarkable increase in the L_D, and L_{sp2} values is achieved by doping/co-doping. For instance, the LrGO, N-LrGO and SN-LrGO exhibited η_D values of 2.26×10^{11}, 1.1×10^{11} and 5.23×10^{10}, respectively. While the L_D values were 15, 22.8, and 32.87 nm and, L_{sp2} values were 25.3, 52.3, and 108.07 nm for LrGO, N-LrGO and SN-LrGO, respectively. Accordingly, the SN co-doping provided a best mean for modulating the structure of LrGO film towards lower defects density and larger size of graphite crystallite and hence more pathways for enhancing the electronic properties of graphene sheets at the atomic level.

The content and bond configurations of dopants on the surface of LrGO sheets were analyzed using XPS and the acquired results are presented in Fig. 4. The wide XPS spectra for the LrGO-based films, Fig. 4 (a), show two major peaks are located at 285 and 532 eV corresponding to the C 1 s and O 1 s binding energies, respectively, and minor two peaks allocated at 164 and 400 eV matching the S 2p and N 1 s binding energies, respectively. The nitrogen content in N-LrGO and SN-LrGO films are found to be 1.98 and 3.71 at. %, respectively. While sulfur content in SN-LrGO film is 1.82 at. %. The simultaneous incorporation of S and N species in the presence of oxygen significantly modifies the surface chemistry of carbon leading to considerably higher doping levels. The synergetic effect between N and S occurs through carbon atoms in neighboring hexagonal rings in a graphene sheet [44,48,61].

The C 1 s high-resolution spectra for LrGO in Fig. 4(b), was deconvoluted and fitted into 4 sub-spectra with peaks located at 284.4, 285.4, 288.1, and 289.8 eV corresponding to C=C in sp^2 domain, C—C in sp^3 domain, C=O and O—C=O. The C1s of N-LrGO Fig. 4(c) was
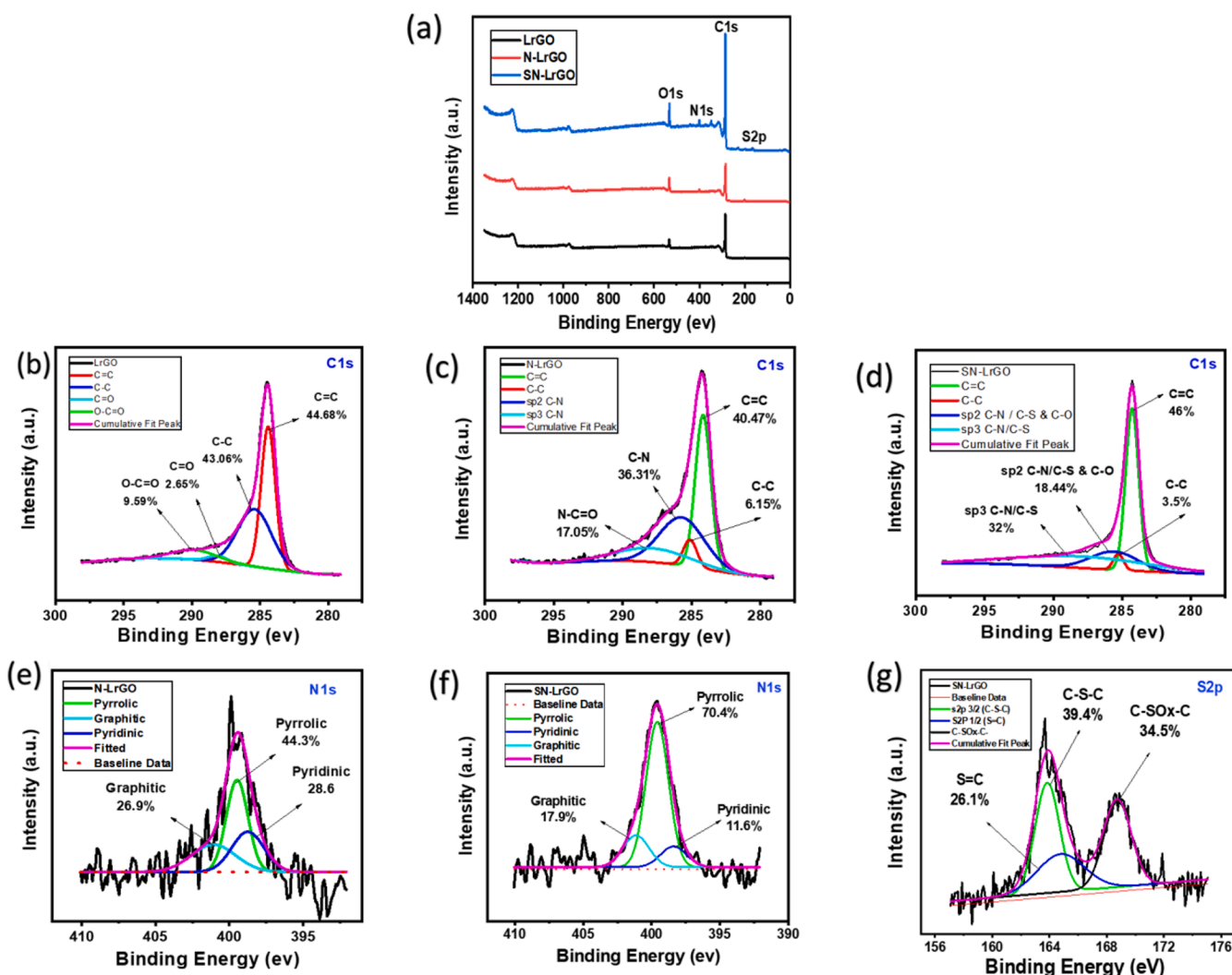
Fig. 4. XPS survey wide spectra for LrGO, N-LrGO and SN-LrGO films (a); High resolution C 1 s spectra from LrGO (b); N-LrGO (c) and SN-rGO (d) films; High resolution N 1 s spectra from N-LrGO (e) and SN-LrGO (f) films; High resolution S 2p spectrum from SN-LrGO sample (g).

deconvoluted into 4 peaks corresponding to C═C Sp2 (284.16 eV), C-C sp3 (285.2 eV), the peak at 285.7 eV is attributed either to C—O or sp2 hybridized C—N, and the peak at 287.2 eV corresponds to C═O or sp3 hybridized C—N bonds that are formed through the C—O—C bonds [62-64]. For SN-LrGO Fig. 4(d), the peaks are located at 284.28, 285.28, 285.6, and 287.8 eV corresponding to sp2 hybridized C═C , sp3 hybridized C—C , sp2 hybridized C—N/C—S/C—O, and C═O or sp3 C—N/C—S bonds that are formed through the C—O—C bonds, respectively [44,65,66]. The sp^3 to sp^2 carbon ratio for LrGO sample is decreased from 0.96 to 0.15 and 0.08 for N-LrGO and SN-LrGO films, respectively. This further confirms the extra recovery of sp^2 carbon domains with the use of urea/thiourea dopant precursors.

The N 1 s high-resolution peak of the N-doped samples, **4(e)** and **(f)**, are deconvoluted into three components at 398.9, 399.9, and 401.8 eV corresponding to pyridinic N, pyrrolic N, and graphitic N species, respectively [64]. In pyridinic N, the N atom is located in sp^2 hybridized bonding with two neighbor C atoms, while in graphitic N, the C atom is substituted by N atom in the basal plane of graphitic sheets. For the pyrrolic N, the N atom is sp^3 hybridized in a five-member ring, which indicate that the pyrrolic N should locate out-of-plan or at the edges of the basal plane of the rGO layer as schematically presented in Fig. 5. The fractions of pyrrolic N, pyridinic N, and graphitic N in the N-LrGO sample are estimated to be 44.35, 28.68, and 26.96%, respectively, and 70, 11.6, and 17.9%, respectively, in the SN-LrGO sample. This indicates

that most of the incorporated nitrogen atoms have the pyrrolic N bonding configuration and its fraction is increased when it is co-doped with sulfur atoms.

The high-resolution of S 2p spectrum is shown in Fig. 4**(g)**. The S 2p peak is deconvoluted into three peaks, namely, S $2p_{3/2}$ (C—S—C) at 163.5 eV corresponding to the thiophene type bond, S $2p_{1/2}$ (S═C) at 164.9 eV, and (sulfoxide) SO_x groups at 168.7 eV [44,66]. Since the atomic size of S is quite larger than that of C and N, the insertion of S in the plan of carbon graphitic lattice is harder than N, and hence the S-configurations are expected to be allocated at the edges of graphene sheet, as illustrated in Fig. 5 [67].

Summarizing the above results, GO prepared by chemical exfoliation approaches can be regarded as O-doped graphene material. The abundant oxygen functional groups and defects in GO can act as reactive sites for the doping of other heteroatoms. A large number of structural defects are produced in the basal plane of rGO sheets with the removal of oxygen functional groups via using the photo thermal reduction technique. Making use of such defected sites, heteroatoms are effectively introduced to the basal plan and active edges of graphitic sheets, Fig. 5. As evidenced by the FTIR and XPS analyses, the doped N and S atoms are covalently bonded in different bonding configurations to the carbon atoms; N (pyrrolic N, graphitic N, and pyridinic N), S (thiophene S, and sulphoxides). The N-doped LrGO film exhibits dominating pyrrolic N, compared to graphitic N and pyridinic N. Because of the similar bond
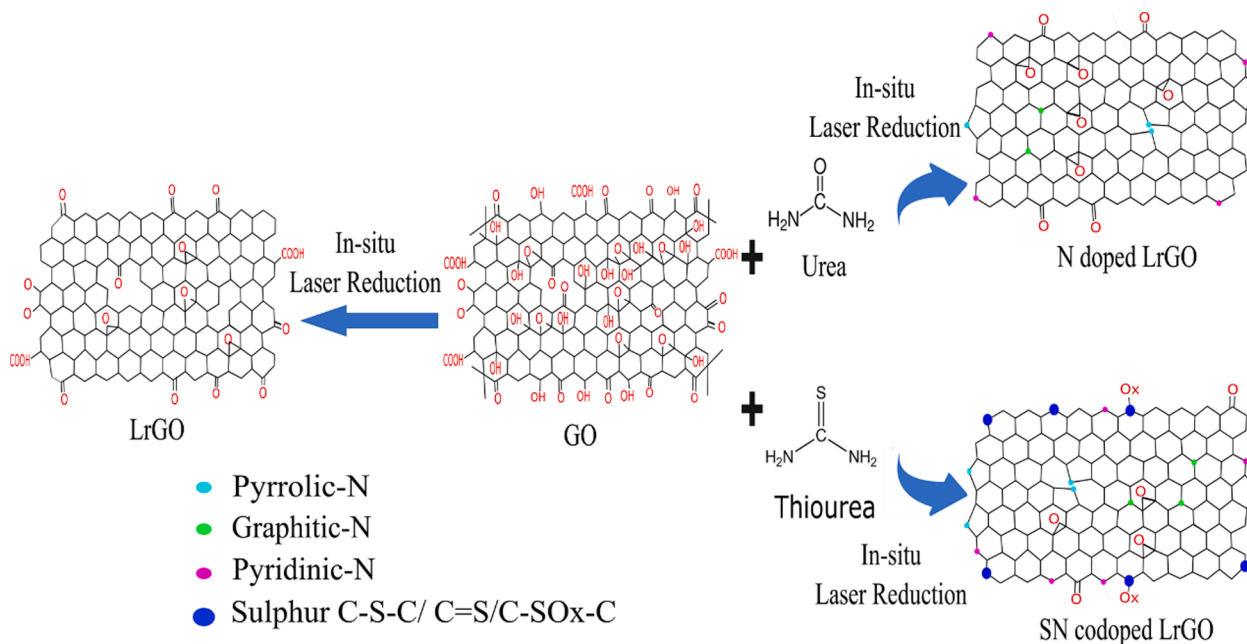
Fig. 5. Schematic representation of in-situ doping with N and SN atoms and laser assisted reduction of the GO-based films.

lengths of C—N (1.41 A) and C—C (1.42 A), the sp^2 bonded pyridinic N and graphitic N configurations exert a marginal strain on the planar structure of the basal plane of graphitic sheets. In contrast, the sp^3 bonded pyrrolic N disrupts the planar structure of graphene and leads to the visible corrugated morphology shown in Fig. 2**(g) and (h)**. The co-doping of N and S atoms create synergistic effects via inducing higher level of N-dopant atoms and promoting more contribution from pyrrolic N, besides sulfurizing the active edges of graphene sheets. These effects seem to release more strain in the basal plane of graphitic sheets and

hence leads to more corrugated morphology, Fig. 2**(h)**. Finally, it worthy to mention that the invasion of N and S dopant atoms the carbon sheets was found not only to incorporate into structural defects of sheets but also intercalate among them, promoting better reduction and exfoliation, and preventing of layer restacking. This produced doped LrGO sheets with a fewer number of graphene layers, lower defects (larger inter-defect distance and lower defects density) and an extra recovery of C=C in sp^2 carbon domains. These results indicate the effectiveness of our novel approach for the in-situ doping/co-doping in the carbon
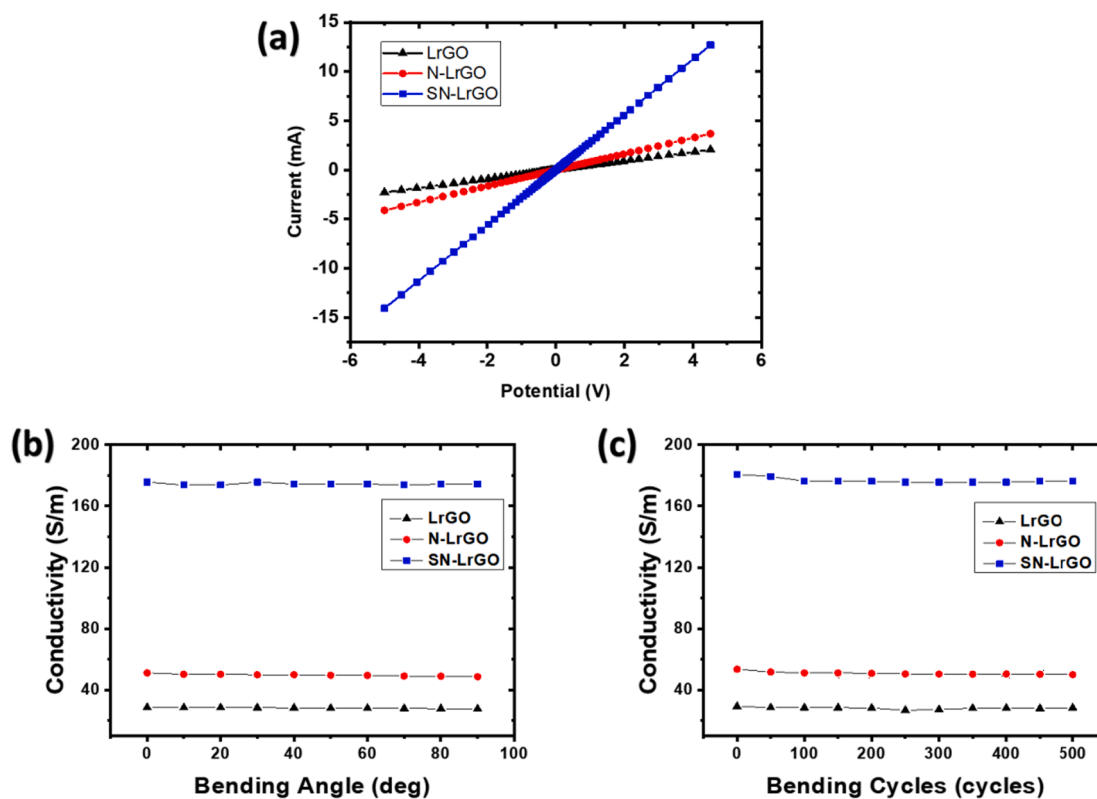

Fig. 6. I-V curves (a); change in conductivity versus bending angle (b); conductivity versus bending cycles up to 500 cycles (c) for LrGO, N-LrGO and SN-LrGO films.

framework of GO via photothermal reduction method.

3.3. Electrical conductivity measurements

The electrical behavior of the reduced films was studied by I-V analysis are shown in Fig. 6. The linear behavior of the I-V curves, Fig. 6 **(a)**, for all films confirms their Ohmic behavior and represents a platform to calculate the electrical conductivities (σ). The deduced σ values for LrGO, N-LrGO, and SN-LrGO films are 28, 51, and 176 Sm^{-1}, respectively. The increase in σ value from LrGO to N-LrGO and SN-LrGO, is attributed to the effect of heteroatoms doping and can be accounted for three contributing factors, namely; an increase in carrier concentration, decrease in defect density and an increase in interconnectivity, and electron mobility between the doped-LrGO sheets. In this regard, the pyrrolic-N and thiophene groups allocated at the edges and out of the basal plane of graphitic sheets, produce more corrugated surface and prevent layer restacking. This results in an increase in interconnectivity,

conjugation of the LrGO sheets and surface area, consequently increasing electron percolation [66,68,69] and hence contribute the observed improvement in the conductivity of SN-LrGO film. In addition, the higher polarizability of S compared to N due to its larger atomic size results in higher tendency of S has to donate electrons, this can be related to the ultimate enhanced conductivity of SN-LrGO film [66].

To verify the flexibility and durability of the films, the electrical conductivity is measured under different bending angles (10°-90°) and cycles. The measured electrical conductivities for the three films impressively remain almost unchanged even at the maximum bending angle of 90°, Fig. 6**(b)**, or after 500 bending cycle at 45° bending angle, Fig. 6**(c)**, revealing the excellent robustness of the films.

3.4. Electrochemical performance of LrGO-based films

To evaluate the impacts of simultaneous reduction, in-situ doping and patterning and on the capacitive performance of pristine LrGO, N-
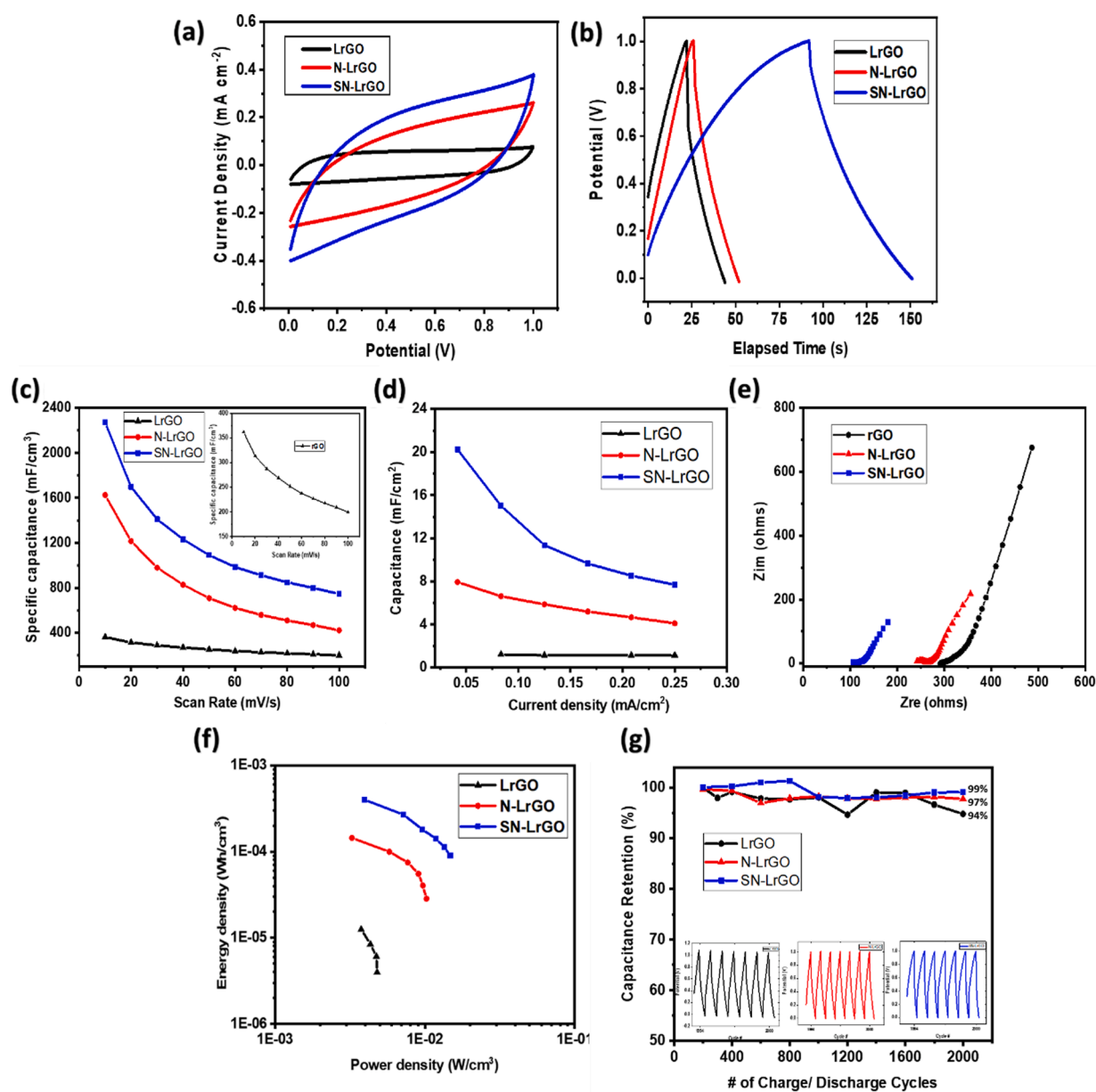

Fig. 7. Electrochemical performance of LrGO, N-LrGO and SN-LrGO; (a) comparative CV profiles at 50 mV S^{-1} (a); charge/discharge curves at current density 0.125 mA.cm^{-2} (b); change in volumetric specific capacitance at different scan rates (c); change in areal Specific capacitance different current densities (d); Nyquist plots in the frequency range 100 kHz–100 mHz (e); Ragone plot (f); Electrochemical Stability performance at current density of 0.125 mA cm^{-2} (g).

LrGO and SN-LrGO films, a series of comparative electrochemical measurements were conducted on symmetric PSC cells made of these films, Fig. 7. Each cell is composed of six interdigitated electrodes and covered with PVA-H_3PO_4 gel electrolyte, as shown in Fig. 1.

The comparative CV curves for the LrGO, N-LrGO and SN-LrGO cells were measured at a scan rate of 50 mV s^{-1}, Fig. 7(a). The CV for the LrGO cell has a rectangular shape typical of EDLC behavior, while those for N-LrGO and the SN-LrGO cells show ellipsoid shape that implies the contribution of extrinsic pseudocapacitive effect aroused from hetero-atoms dopants. Additionally, the CV curves for the cells made from doped LrGO films, particularly SN-LrGO cell, have larger enclosed integration areas than that delivered by LrGO cell, demonstrating the superiority of doped-LrGO cells as PSCs. This is in an agreement with previous reports that indicated doping of graphene with heteroatoms beneficially creates an extrinsic pseudocapacitive effect, which enhances carriers concentrations, electrons transfer, and improves wetta-bility of graphene in an aqueous electrolyte [44,48,70,71].

The galvanic charge–discharge (GCD) profiles of the fabricated cells were also measured at a current density of 0.125 mAcm^{-2}, Fig. 7(b). The profile for LrGO cell shows a symmetric triangular form, implying the dominance of EDLC as the main capacitive mechanism. The profiles for the N-LrGO and SN-LrGO cells show a slight curvature, less steepness and lower IR drop along with an increase in the discharge time in their discharge curves, confirming the Faradic contribution of heteroatoms in the capacitive mechanism and reduction of the overall internal cell resistance. The variations in extracted specific capacitance volumetric (C_V) and areal (C_a) versus scan rates and the discharge current densities are plotted in Fig. 7(c) and (d), respectively. As seen, capacitance values are typically decreased with increasing the current density and scan rate. Quantitatively, SN-LrGO PSC manifests the highest value of C_a that equals to 11.35 mF cm^{-2} (C_v 1.8F cm^{-3}) at a current density of 0.125 mA cm^{-2}, whereas N-LrGO and LrGO recorded 5.87 mF cm^{-2} (C_v 0.9 F cm^{-3}) and 1.15 mF cm^{-2} (C_v 0.15F cm^{-3}), respectively.

On the other hand, the N-LrGO and the SN-LrGO cells show, supplementary information Fig. S3, wider current densities measuring range from 0.029 mA cm^{-2} up to 0.2 mA cm^{-2} higher than that for the LrGO cell (0.029 mA cm^{-2} up to 0.125 mA cm^{-2}). This indicates the higher rate capabilities and improved columbic efficiencies of the doped-LrGO cells, particularly the SN-LrGO cell, such that they can effectively charging and discharging at low current density as well as high current density.The higher capacitive performance for the doped samples correlates to the pseudocapacitance effect resulting from pyrrolic N and the reversible redox reactions of the sulfur dopant species (sulfone and sulfoxides) in addition to their effect on the improved wettability of graphene [44,48,61].

On the other hand, The EIS measurement was also used to better understand the electronic and ionic conductivities of the fabricated PSC cells. Nyquist plots of the three cells acquired in the frequency range 100 kHz–100 mHz are shown in Fig. 7(e). The Nyquist plots are consisting of a high-frequency region semicircle and a low-frequency linear part with approximately 45° declination angle for the Warburg imped-ance (Z_W), which is the typical plot for porous electrode used in energy storage application [41,42]. The intersection of the high-frequency part of the plot with real impedance x-axis represents the equivalent series resistance (R_{ESR}) which is accounted for the ionic resistance of the electrolyte, the intrinsic resistance of the active material, and the contact resistance at the interface between the active material and the current collector. The diameter of the semicircle is corresponding to the charge transfer resistance (R_{ct}) caused by the charge transfer process at the electrode/electrolyte interface. The estimated R_{ESR} values for the cells with LrGO, N-LrGO, and SN-LrGO electrodes are 301, 262, and 114 Ω, respectively. Meanwhile, the deduced R_{ct} values for the LrGO, N-LrGO and SN-LrGO cells are 31, 20 and 7 Ω respectively. This confirms the easier charge and electron transfer across doped-LrGO/electrolyte interfaces than at pristine LrGO/electrolyte interfaces. These results are in full agreement with our findings from XPS where the larger

content of pyrrolic N in the doped and co-doped films contributes to the improved wettability of graphene [44].

Ragone plot is a relation between the volumetric energy (E_v) and the volumetric power (P_v) densities that examined over a wide range of charge/discharge current densities, Fig. 7(f). Obviously, the energy storage of the SN-LrGO cell is located at the top right of the Ragone plot, outperforming those of the N-LrGO and LrGO cells. For instance, at 0.125 mA cm^{-2} a maximum energy density of 0.4 mWh cm^{-3} vs a power density 3.95 mW cm^{-3} is obtained for the SN-LrGO cell, which is higher than 0.144 mWh cm^{-3} vs 3.26 mW cm^{-3} and 0.0125 mWh cm^{-3} vs 3.76 mW cm^{-3} for the N-LrGO and LrGO cells, respectively.

The overall performance of the fabricated cells was further investigated by measuring their electrochemical stability. Fig. 7(g) presents the cycle stability test of PSCs cells through frequent charging and discharging up to 2000 cycles at current density of 0.125 mAcm^{-2}. The insets of Fig. 7(g) display the last 6 charging and discharging cycles of each cell. After 2000 cycles, the SN-LrGO, N-LrGO, and LrGO cells retained 99.2, 97.0 and 94% of their initial capacitances, respectively, with no apparent distortion in shape of the last tested charge/discharge cycles.

In brief, the enhancements in the electrochemical capacitances of LrGO film by N doping and SN co-doping are attributed to the synergism between the EDLC and pseudo-capacitance mechanisms [49]. The contribution of the EDLC comes from the increase in the electrical aspects of the unique graphene framework, while the contribution of the pseudo-capacitance is stemming from the Faradaic redox reaction between non graphitic bonding configurations (pyrrolic-N, and sulfoxides species) of dopants and the ions of the electrolyte [34,44,67]. Moreover, the outstanding electrochemical stability indicates that the novel laser assisted doping method of the LrGO film presented here enhances not only the electrical and the electrochemical properties of the LrGO-based devices, but also promotes the durability and reversibility of the fabricated cells. A summary for the electrochemical testing results of the three cells is summarized in Table 1, where it reveals that the SN-LrGO cell exhibits the best performance. Furthermore, SN-LrGO cell was able to maintain similar capacitive performance after severe and continual bending, supplementary information Fig. S4.

To put these results in perspective with current research, we have compared our results to previously reported results of micro-supercapacitors and the results are summarized in **Table S2**. Interestingly, the outstanding results achieved from our developed devices especially the areal capacitance C_a are superior to the reported values in literature for EDLC micro-PSC, with values in the range of 0.4–2 mFcm^{-2} [30,72,73]. For instance, the C_a attained by the SN-LrGO PSC is superior to values previously reported for EDLC, pseudo-, and hybrid micro supercapacitors: 1.7 mF/cm^2 for carbon onions [74], Laser scribed graphene PSC (2.32 mF cm^{-2}) [30], oxygen plasma (3 mF cm^{-2} for Holey-PANI/exfoliated graphene) [75], 2.16–5.1 mF/cm^2 graphene–CNT [76,77], 4.76 mF/cm^2 for vanadium disulfide nanosheets [78], and 8 mF/cm^2 for molybdenum disulfide [79] and even comparable to that laser-induced graphene (16.5 mF cm^{-2} for B-LIG) [35] fabricated in the micro-scale and with a much thinner thickness ~ 25 μm. Although, and due to resolution limitations of the commercial CO_2 laser engraving machine, we couldn't obtain an interspacing of interdigitated electrodes

Table 1

Summary of electrochemical parameters for the fabricated cells. The specific capacitance, energy density and maximum power density were calculated with 6-interdigitated electrodes at 0.125 mA cm^{-2}.

PSC	LrGO	N-LrGO	SN-LrGO
C_v (mF cm^{-3})	152	916	1801
C_a (mF cm^{-2})	1.15	5.87	11.35
R_{ESR} (Ω)	301	262	114
R_{ct} (Ω)	7	20	31
E_V (mWh cm^{-3})	7.5×10^{-3}	0.074	0.18
P_V (mW cm^{-3})	7.23	24.5	48.6

below 1 mm, but we were able to obtain remarkable high values for the capacitance, and retention rates with our developed materials. However, we believe that the simple approach presented in this study for the simultaneous doping and reduction of GO supported on flexible substrates opens a way for large scale production of efficient graphene-based flexible storage devices. The rate capability and the power density for such devices suggested to be greatly improved if an interspacing in micrometer scale can be reached using high-resolution laser systems as well as the employment of ionic liquid electrolytes [30].

To realize a miniaturized cell of SN-LrGO PSC and to obtain good control over the voltage and current output, the effects of changing the number of the interdigitated electrodes per unit area along with series and parallel combinations of PSCs were investigated. The impact of changing the number of the interdigitated electrodes per unit area on the capacitive performance of the SN-LrGO cell was investigated. Four interdigitated architectures composed of 4, 6, 8 and 10 electrodes were studied. The interspacing between these fingers was fixed at 1 mm, while the width of the fingers varied accordingly, supplementary information Fig. S5 and S6. According to previous reports, increasing the number of electrodes per footprint area typically enables a larger access area for the electrolyte along with a reduction in the average migration distance for the ions and an increase in the electron transfer dynamics [30,39]. SN-LrGO PSC composed of 10 fingers achieved an areal capacitance (C_a) equals to 13.8 mF cm^{-2} calculated at 10 mV S^{-1}, which translates to C_v value of 2195 mF cm^{-3}. These values are significantly higher than those of the 4 fingers cell with C_a equals to 8.3mF cm^{-2} and C_v is1320 mF cm^{-3}.

In order to obtain good control over the voltage and current output and to meet the desired requirements by different applications, series and parallel combinations of PSCs are usually suited to increase the operating voltage window, stored energy, and the discharge time [80]. For this regard, we employed our novel technique to fabricate a flexible and lightweight power bank array composed of series (S) and parallel (P) combinations of SN-LrGO cells, with 6 interdigitated electrodes, seeking higher voltage ratings. Using the CO_2 laser reduction technique, an array based on SN-LrGO and composed of nine cells (3 cells connected in series × 3 cells in parallel) was directly fabricated in a single step as schematically presented in Fig. 8(a). The CV curves of single cell,

3 cells connected in series (3S), 3 cells connected in parallel (3P), and the whole nine cells array (3Sx 3P), Fig. 8(b), were traced at 100 mV s^{-1} and the corresponding GCD profiles are shown in Fig. 8(c). As seen, the operating voltage window was extended to 3 V for 3S cells and the (3S × 3P) bank compared to 1 V for the single cell. Also, the parallel combinations enhance the capacitance behavior such that the enclosed area within CV curve was increased significantly for the 3P and the (3Sx3P) bank. Additionally, the discharge time was increased to ~ 4 times that of a single cell, whereas the IR drop was decreased significantly upon the parallel combination of the SN-LrGO cells. In Fig. 8(d), 4S cells were used to light a Red LED. Thus, the attained results firmly confirm the flexibility and the controllability of our novel method for the fast production of flexible and highly-performance supercapacitor arrays for span of different applications.

4. Conclusions

In conclusion, we have developed a single-step and low-cost fabrication approach for the real-time doping, reduction, and patterning of flexible GO/PET under ambient conditions for planar supercapacitors (PSCs). The method negates the need for high synthesis temperature and aggressive chemicals associated with current existing doping methods. The doped (N-LrGO) and co-doped (SN-LrGO) electrodes can be scalably produced and exhibited high N atoms and SN atoms contents, respectively, and lower structural defects which result in outstanding enhancements in the electrical and electrochemical performances compared to the pristine LrGO electrode. The electrochemical results showed that the areal specific capacitance and the volumetric energy density of the SN-LrGO-based PSC at different power density significantly outperforming those of N-LrGO and LrGO at different current and power densities. A maximum performance of an areal specific capacitance of 13.8 mF cm^{-2} and a high-power density of 151.7mW cm^{-3} at an energy density of 0.152 mWh cm^{-3} are achieved with PSC comprises 10 interdigitated electrodes at 1 mm interspacing. Besides, the stability and bending tests showed outstanding flexibility and capacitance retention for the SN-LrGO device which showed no apparent change in its intrinsic electrical conductivity and sustained more than 99% of initial capacitance after 2000 cycling test. Furthermore, the versatility of our novel
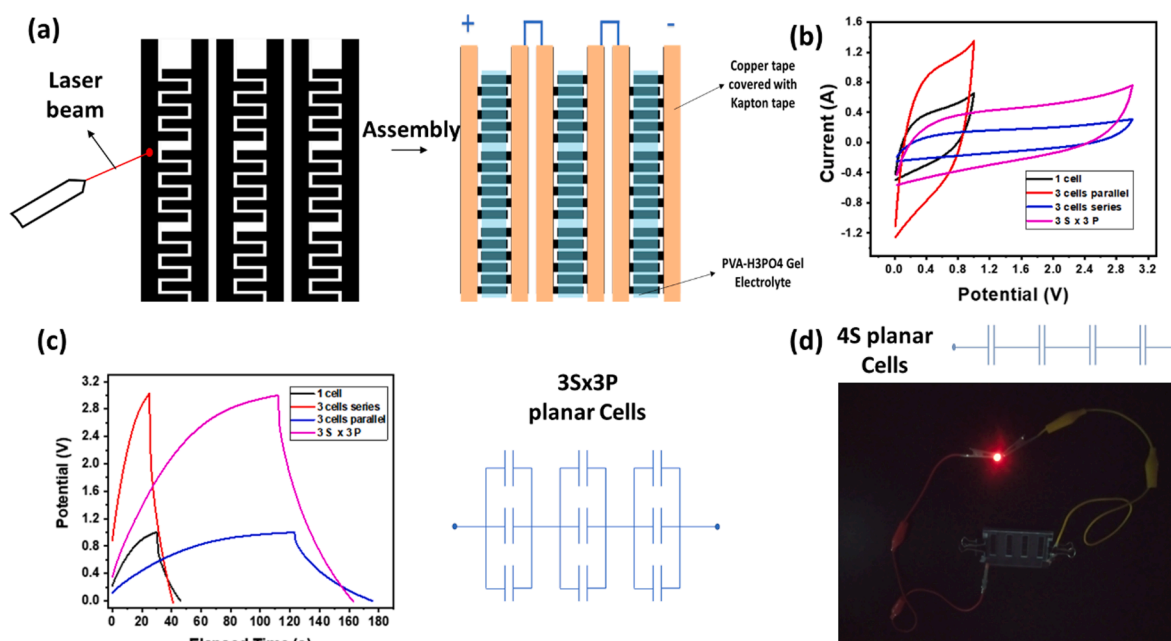

Fig. 8. Fabrication process for an array of 9 cells connected in series (S),parallel (P) and (3P × 3 Ss) combinations (a); CV curves measured at 100 mVs^{-1}(b), GCD profiles (c), for a single cell, 3 cells connected in series (3S), 3 cells connected in parallel (3P), and 3Sx3P array, a Red LED is lightened by a 4S array (d). (For interpretation of the references to colour in this figure legend, the reader is referred to the web version of this article.)

developed technique was successfully tested in the fast fabrication of a complete array encompass nine PSC device. In principle, the devised technique is considered promising for mass production of flexible heteroatom doped-LrGO films with tailored properties having great application prospects.

CRediT authorship contribution statement

Aya Hamed: Methodology, Validation, Investigation, Visualization, Writing - review & editing. **Amr Hessein:** Methodology, Writing - review & editing. **Ahmed Abd El-Moneim:** Writing - review & editing, Supervision.

Declaration of Competing Interest

The authors declare that they have no known competing financial interests or personal relationships that could have appeared to influence the work reported in this paper.

Data availability

The raw data required to reproduce these findings are available to download from https://doi.org/10.17632/8h8zggfnrh.1.

Appendix A. Supplementary material

Supplementary data to this article can be found online at https://doi.org/10.1016/j.apsusc.2021.149457.

References

[1] M. Salanne, B. Rotenberg, K. Naoi, K. Kaneko, P.-L. Taberna, C.P. Grey, B. Dunn, P. Simon, Efficient storage mechanisms for building better supercapacitors, Nat. Energy 1 (2016) 16070, https://doi.org/10.1038/nenergy.2016.70.
[2] W.K. Chee, H.N. Lim, Z. Zainal, N.M. Huang, I. Harrison, Y. Andou, Flexible Graphene-Based Supercapacitors: A Review, J. Phys. Chem. C 120 (2016) 4153–4172, https://doi.org/10.1021/acs.jpcc.5b10187.
[3] Khosrozadeh, A.; Xing, M.; Wang, Q. A high-capacitance solid-state supercapacitor based on free-standing film of polyaniline and carbon particles. Appl. Energy 2014, 153, 87–93, doi:j.apenergy.2014.08.046.
[4] S. Hassan, M. Suzuki, S. Mori, A.A. El-Moneim, MnO 2 /carbon nanowall electrode for future energy storage application: effect of carbon nanowall growth period and MnO 2 mass loading, RSC Adv. 4 (2014) 20479–20488, https://doi.org/10.1039/C4RA01132E.
[5] K. Guo, Y. Wan, N. Yu, L. Hu, T. Zhai, H. Li, Hand-drawing patterned ultra-thin integrated electrodes for flexible micro supercapacitors, Energy Storage Mater. 11 (2018) 144–151, https://doi.org/10.1016/j.ensm.2017.10.009.
[6] J.-Q. Xie, Y.-Q. Ji, J.-H. Kang, J.-L. Sheng, D.-S. Mao, X.-Z. Fu, R. Sun, C.-P. Wong, In situ growth of Cu(OH) 2 @FeOOH nanotube arrays on catalytically deposited Cu current collector patterns for high-performance flexible in-plane micro-sized energy storage devices, Energy Environ. Sci. 12 (2019) 194–205, https://doi.org/10.1039/C8EE01979G.
[7] J. Lee, J.Y. Seok, S. Son, M. Yang, B. Kang, High-energy, flexible micro-supercapacitors by one-step laser fabrication of a self-generated nanoporous metal/oxide electrode, J. Mater. Chem. A 5 (2017) 24585–24593, https://doi.org/10.1039/C7TA07960E.
[8] Y. Yang, L. He, C. Tang, P. Hu, X. Hong, M. Yan, Y. Dong, X. Tian, Q. Wei, L. Mai, Improved conductivity and capacitance of interdigital carbon microelectrodes through integration with carbon nanotubes for micro-supercapacitors, Nano Res. 9 (2016) 2510–2519, https://doi.org/10.1007/s12274-016-1137-3.
[9] Q. Jiang, N. Kurra, C. Xia, H.N. Alshareef, Hybrid Microsupercapacitors with Vertically Scaled 3D Current Collectors Fabricated using a Simple Cut-and-Transfer Strategy, Adv. Energy Mater. 7 (2017) 1601257, https://doi.org/10.1002/aenm.201601257.
[10] L. Liu, Q. Lu, S. Yang, J. Guo, Q. Tian, W. Yao, Z. Guo, V.A.L. Roy, W. Wu, All-Printed Solid-State Microsupercapacitors Derived from Self-Template Synthesis of Ag@PPy Nanocomposites, Adv. Mater. Technol. 3 (2018) 1700206, https://doi.org/10.1002/admt.201700206.
[11] Z. Liu, Z.-S. Wu, S. Yang, R. Dong, X. Feng, K. Müllen, Ultraflexible In-Plane Micro-Supercapacitors by Direct Printing of Solution-Processable Electrochemically Exfoliated Graphene, Adv. Mater. 28 (2016) 2217–2222, https://doi.org/10.1002/adma.201505304.
[12] H. Huang, X. Chu, H. Su, H. Zhang, Y. Xie, W. Deng, N. Chen, F. Liu, H. Zhang, B. Gu, W. Deng, W. Yang, Massively manufactured paper-based all-solid-state flexible micro-supercapacitors with sprayable MXene conductive inks, J. Power Sources 415 (2019) 1–7, https://doi.org/10.1016/j.jpowsour.2019.01.044.
[13] L. Li, Z. Lou, W. Han, D. Chen, K. Jiang, G. Shen, Highly Stretchable Micro-Supercapacitor Arrays with Hybrid MWCNT/PANI Electrodes, Adv. Mater. Technol. 2 (2017) 1600282, https://doi.org/10.1002/admt.201600282.
[14] A.A. El-Moneim, J. Bhattarai, Z. Kato, K. Izumiya, N. Kumagai, K. Hashimoto, Mn-Mo-Sn Oxide Anodes for Oxygen Evolution in Seawater Electrolysis for Hydrogen Production, ECS Trans. 25 (2019) 127–137, https://doi.org/10.1149/1.3422589.
[15] X. Wang, G. Shi, An introduction to the chemistry of graphene, Phys. Chem. Chem. Phys. 17 (2015) 28484–28504, https://doi.org/10.1039/C5CP05212B.
[16] M., A.; Paul, A. Importance of Electrode Preparation Methodologies in Supercapacitor Applications. ACS Omega 2017, 2, 8039–8050, doi:10.1021/acsomega.7b01275.
[17] C. Liu, Z. Yu, D. Neff, A. Zhamu, B.Z. Jang, Graphene-Based Supercapacitor with an Ultrahigh Energy Density, Nano Lett. 10 (2010) 4863–4868, https://doi.org/10.1021/nl102661q.
[18] A. González, E. Goikolea, J.A. Barrena, R. Mysyk, Review on supercapacitors: Technologies and materials, Renew. Sustain. Energy Rev. 58 (2016) 1189–1206, https://doi.org/10.1016/j.rser.2015.12.249.
[19] M. Gamil, H. Nageh, I. Bkrey, S. Sayed, A.M.R.F. El-bab, K. Nakamura, O. Tabata, A.A. El-moneim, Graphene-Based Strain Gauge on a Flexible Substrate, Sensors Mater. 26 (2014) 699, https://doi.org/10.18494/SAM.2014.1030.
[20] K.M. El-Khatib, M.O. Abou Helal, A.A. El-Moneim, H. Tawfik, Corrosion stability of SUS316L HVOF sprayed coatings as lightweight bipolar plate materials in PEM fuel cells, Anti-Corrosion Meth. Mater. 51 (2004) 136–142, https://doi.org/10.1108/00035590410523238.
[21] S. Sayed, M. Gamil, A.F. El-Bab, K. Nakamura, T. Tsuchiya, O. Tabata, A.A. El-Moneim, Graphene film development on flexible substrate using a new technique: Temperature dependency of gauge factor for graphene-based strain sensors, Sens. Rev. 36 (2016) 140–147, https://doi.org/10.1108/SR-07-2015-0114.
[22] M. Gamil, O. Tabata, K. Nakamura, A.M.R.F. El-Bab, A.A. El-Moneim, Investigation of a new high sensitive micro-electromechanical strain gauge sensor based on graphene piezoresistivity, in: Key Engineering Materials, Trans Tech Publications Ltd, 2014, pp. 207–210.
[23] Z. Wan, S. Wang, B. Haylock, J. Kaur, P. Tanner, D. Thiel, R. Sang, I.S. Cole, X. Li, M. Lobino, Q. Li, Tuning the sub-processes in laser reduction of graphene oxide by adjusting the power and scanning speed of laser, Carbon N. Y. 141 (2019) 83–91, https://doi.org/10.1016/j.carbon.2018.09.030.
[24] R. Arul, R.N. Oosterbeek, J. Robertson, G. Xu, J. Jin, M.C. Simpson, The mechanism of direct laser writing of graphene features into graphene oxide films involves photoreduction and thermally assisted structural rearrangement, Carbon N. Y. 99 (2016) 423–431, https://doi.org/10.1016/j.carbon.2015.12.038.
[25] L. Guo, R.-Q. Shao, Y.-L. Zhang, H.-B. Jiang, X.-B. Li, S.-Y. Xie, B.-B. Xu, Q.-D. Chen, J.-F. Song, H.-B. Sun, Bandgap Tailoring and Synchronous Microdevices Patterning of Graphene Oxides, J. Phys. Chem. C 116 (2012) 3594–3599, https://doi.org/10.1021/jp209843m.
[26] T.X. Tran, H. Choi, C.H. Che, J.H. Sul, I.G. Kim, S.-M. Lee, J.-H. Kim, J. In, Bin Laser-Induced Reduction of Graphene Oxide by Intensity-Modulated Line Beam for Supercapacitor Applications, ACS Appl. Mater. Interf. 10 (2018) 39777–39784, https://doi.org/10.1021/acsami.8b14678.
[27] Y. Zhang, L. Guo, S. Wei, Y. He, H. Xia, Q. Chen, H.-B. Sun, F.-S. Xiao, Direct imprinting of microcircuits on graphene oxides film by femtosecond laser reduction, Nano Today 5 (2010) 15–20, https://doi.org/10.1016/j.nantod.2009.12.009.
[28] Y.-L. Zhang, Q.-D. Chen, H. Xia, H.-B. Sun, Designable 3D nanofabrication by femtosecond laser direct writing, Nano Today 5 (2010) 435–448, https://doi.org/10.1016/j.nantod.2010.08.007.
[29] M.F. El-Kady, V. Strong, S. Dubin, R.B. Kaner, Laser Scribing of High-Performance and Flexible Graphene-Based Electrochemical Capacitors, Science (80-.) 335 (2012) 1326–1330, https://doi.org/10.1126/science.1216744.
[30] M.F. El-Kady, R.B. Kaner, Scalable fabrication of high-power graphene micro-supercapacitors for flexible and on-chip energy storage, Nat. Commun. 4 (2013) 1475, https://doi.org/10.1038/ncomms2446.
[31] J. Liang, A.K. Mondal, D.-W. Wang, F. Iacopi, Graphene-Based Planar Microsupercapacitors: Recent Advances and Future Challenges, Adv. Mater. Technol. 4 (2019) 1800200, https://doi.org/10.1002/admt.201800200.
[32] T. Kuila, S. Bose, A.K. Mishra, P. Khanra, N.H. Kim, J.H. Lee, Chemical functionalization of graphene and its applications, Prog. Mater. Sci. 57 (2012) 1061–1105, https://doi.org/10.1016/j.pmatsci.2012.03.002.
[33] X. Wang, G. Sun, P. Routh, D.-H. Kim, W. Huang, P. Chen, Heteroatom-doped graphene materials: syntheses, properties and applications, Chem. Soc. Rev. 43 (2014) 7067–7098, https://doi.org/10.1039/C4CS00141A.
[34] Y. Zhou, X. Xu, B. Shan, Y. Wen, T. Jiang, J. Lu, S. Zhang, D.P. Wilkinson, J. Zhang, Y. Huang, Tuning and understanding the supercapacitance of heteroatom-doped graphene, Energy Storage Mater. 1 (2015) 103–111, https://doi.org/10.1016/j.ensm.2015.09.002.

[35] Z. Peng, R. Ye, J.A. Mann, D. Zakhidov, Y. Li, P.R. Smalley, J. Lin, J.M. Tour, Flexible Boron-Doped Laser-Induced Graphene Microsupercapacitors, ACS Nano 9 (2015) 5868–5875, https://doi.org/10.1021/acsnano.5b00436.

[36] A. Lamberti, F. Perrucci, M. Caprioli, M. Serrapede, M. Fontana, S. Bianco, S. Ferrero, E. Tresso, New insights on laser-induced graphene electrodes for flexible supercapacitors: tunable morphology and physical properties, Nanotechnology 28 (2017), 174002, https://doi.org/10.1088/1361-6528/aa6615.

[37] Hummers, W. S.; Offeman, R. E. Preparation of Graphitic Oxide. J. Am. Chem. Soc. 1958, 80, 1339–1339, doi:10.1021/ja01539a017.

[38] M. Wojtoniszak, X. Chen, R.J. Kalenczuk, A. Wajda, J. Łapczuk, M. Kurzewski, M. Drozdzik, P.K. Chu, E. Borowiak-Palen, Synthesis, dispersion, and cytocompatibility of graphene oxide and reduced graphene oxide, Colloids Surf. B Biointerf. 89 (2012) 79–85, https://doi.org/10.1016/j.colsurfb.2011.08.026.

[39] E. Ghoniem, S. Mori, A. Abdel-Moniem, Low-cost flexible supercapacitors based on laser reduced graphene oxide supported on polyethylene terephthalate substrate, J. Power Sources 324 (2016) 272–281, https://doi.org/10.1016/j.jpowsour.2016.05.069.

[40] Q. Chen, X. Li, X. Zang, Y. Cao, Y. He, P. Li, K. Wang, J. Wei, D. Wu, H. Zhu, Effect of different gel electrolytes on graphene-based solid-state supercapacitors, RSC Adv. 4 (2014) 36253–36256, https://doi.org/10.1039/C4RA05553E.

[41] J. Zhang, X.S. Zhao, On the Configuration of Supercapacitors for Maximizing Electrochemical Performance, ChemSusChem 5 (2012) 818–841, https://doi.org/10.1002/cssc.201100571.

[42] S. Zhang, N. Pan, Supercapacitors Performance Evaluation, Adv. Energy Mater. 5 (2015) 1401401, https://doi.org/10.1002/aenm.201401401.

[43] S. Delacroix, H. Wang, T. Heil, V. Strauss, Laser-Induced Carbonization of Natural Organic Precursors for Flexible Electronics, Adv. Electron. Mater. 2000463 (2020) 1–8, https://doi.org/10.1002/aelm.202000463.

[44] T. Wang, L.-X. Wang, D.-L. Wu, W. Xia, D.-Z. Jia, Interaction between Nitrogen and Sulfur in Co-Doped Graphene and Synergetic Effect in Supercapacitor, Sci. Rep. 5 (2015) 9591, https://doi.org/10.1038/srep09591.

[45] R.A. Rochman, S. Wahyuningsih, A.H. Ramelan, Q.A. Hanif, Preparation of nitrogen and sulphur Co-doped reduced graphene oxide (rGO-NS) using N and S heteroatom of thiourea, IOP Conf. Ser. Mater. Sci. Eng. 509 (2019), 012119, https://doi.org/10.1088/1757-899X/509/1/012119.

[46] M.P. Kumar, T. Kesavan, G. Kalita, P. Ragupathy, T.N. Narayanan, D.K. Pattanayak, On the large capacitance of nitrogen doped graphene derived by a facile route, RSC Adv. 4 (2014) 38689–38697, https://doi.org/10.1039/C4RA04927F.

[47] N.M.S. Hidayah, W.-W. Liu, C.-W. Lai, N.Z. Noriman, C.-S. Khe, U. Hashim, H. C. Lee, Comparison on graphite, graphene oxide and reduced graphene oxide: Synthesis and characterization, AIP Conference Proc. 1892 (2017), 150002.

[48] Z. Ouyang, Y. Lei, Y. Chen, Z. Zhang, Z. Jiang, J. Hu, Y. Lin, Preparation and Specific Capacitance Properties of Sulfur, Nitrogen Co-Doped Graphene Quantum Dots, Nanoscale Res. Lett. 14 (2019) 219, https://doi.org/10.1186/s11671-019-3045-4.

[49] H. Xie, C. Hou, H. Wang, Q. Zhang, Y. Li, S, N Co-Doped Graphene Quantum Dot/TiO2 Composites for Efficient Photocatalytic Hydrogen Generation, Nanoscale Res. Lett. 12 (2017) 400, https://doi.org/10.1186/s11671-017-2101-1.

[50] D. Qu, M. Zheng, P. Du, Y. Zhou, L. Zhang, D. Li, H. Tan, Z. Zhao, Z. Xie, Z. Sun, Highly luminescent S, N co-doped graphene quantum dots with broad visible absorption bands for visible light photocatalysts, Nanoscale 5 (2013) 12272, https://doi.org/10.1039/c3nr04402e.

[51] A.C. Ferrari, Raman spectroscopy of graphene and graphite: Disorder, electron–phonon coupling, doping and nonadiabatic effects, Solid State Commun. 143 (2007) 47–57, https://doi.org/10.1016/j.ssc.2007.03.052.

[52] A.C. Ferrari, J.C. Meyer, V. Scardaci, C. Casiraghi, M. Lazzeri, F. Mauri, S. Piscanec, D. Jiang, K.S. Novoselov, S. Roth, A.K. Geim, Raman Spectrum of Graphene and Graphene Layers, Phys. Rev. Lett. 97 (2006), 187401, https://doi.org/10.1103/PhysRevLett.97.187401.

[53] A.C. Ferrari, D.M. Basko, Raman spectroscopy as a versatile tool for studying the properties of graphene, Nat. Nanotechnol. 8 (2013) 235–246, https://doi.org/10.1038/nnano.2013.46.

[54] S. Niyogi, E. Bekyarova, M.E. Itkis, H. Zhang, K. Shepperd, J. Hicks, M. Sprinkle, C. Berger, C.N. Lau, W.A. DeHeer, E.H. Conrad, R.C. Haddon, Spectroscopy of Covalently Functionalized Graphene, Nano Lett. 10 (2010) 4061–4066, https://doi.org/10.1021/nl1021128.

[55] Nguyen, V. T.; Le, H. D.; Nguyen, V. C.; Ngo, T. T. T.; Le, D. Q.; Nguyen, X. N.; Phan, N. M. Synthesis of multi-layer graphene films on copper tape by atmospheric pressure chemical vapor deposition method. Adv. Nat. Sci. Nanosci. Nanotechnol. 2013, 4, doi:10.1088/2043-6262/4/3/035012.

[56] R. Sharma, N. Chadha, P. Saini, Determination of defect density, crystallite size and number of graphene layers in graphene analogues using X-ray diffraction and Raman spectroscopy, Indian J. Pure Appl. Phys. 55 (2017) 625–629.

[57] A.C. Ferrari, J. Robertson, Raman spectroscopy of amorphous, nanostructured, diamond-like carbon, and nanodiamond, Philos. Trans. R. Soc. A Math. Phys. Eng. Sci. 362 (2004) 2477–2512, https://doi.org/10.1098/rsta.2004.1452.

[58] L.G. Cançado, A. Jorio, E.H.M. Ferreira, F. Stavale, C.A. Achete, R.B. Capaz, M.V. O. Moutinho, A. Lombardo, T.S. Kulmala, A.C. Ferrari, Quantifying Defects in Graphene via Raman Spectroscopy at Different Excitation Energies, Nano Lett. 11 (2011) 3190–3196, https://doi.org/10.1021/nl201432g.

[59] A. Das, S. Pisana, B. Chakraborty, S. Piscanec, S.K. Saha, U.V. Waghmare, K. S. Novoselov, H.R. Krishnamurthy, A.K. Geim, A.C. Ferrari, A.K. Sood, Monitoring

[60] dopants by Raman scattering in an electrochemically top-gated graphene transistor, Nat. Nanotechnol. 3 (2008) 210–215, https://doi.org/10.1038/nnano.2008.67.

[60] A. Jorio, Raman Spectroscopy in Graphene-Based Systems: Prototypes for Nanoscience and Nanometrology, ISRN Nanotechnol. 2012 (2012) 1–16, https://doi.org/10.5402/2012/234216.

[61] Y. Zhu, J. Cui, S. An, Z. Li, Y. Zhang, W. He, Facile preparation of sulfur/nitrogen co-doped graphene coupled with Ni(OH)2 for battery-type electrode with superior electrochemical performance, J. Alloys Compd. 810 (2019), 151932, https://doi.org/10.1016/j.jallcom.2019.151932.

[62] Z. Mou, X. Chen, Y. Du, X. Wang, P. Yang, S. Wang, Forming mechanism of nitrogen doped graphene prepared by thermal solid-state reaction of graphite oxide and urea, Appl. Surf. Sci. 258 (2011) 1704–1710, https://doi.org/10.1016/j.apsusc.2011.10.019.

[63] S.J. Hartmann, A.A. Iurchenkova, T. Kallio, E.O. Fedorovskaya, Electrochemical properties of nitrogen and oxygen doped reduced graphene oxide, Energies 13 (2020) 1–14, https://doi.org/10.3390/en13020312.

[64] T. Van Khai, H.G. Na, D.S. Kwak, Y.J. Kwon, H. Ham, K.B. Shim, H.W. Kim, Significant enhancement of blue emission and electrical conductivity of N-doped graphene, J. Mater. Chem. 22 (2012) 17992, https://doi.org/10.1039/c2jm33194b.

[65] W. Ai, Z. Luo, J. Jiang, J. Zhu, Z. Du, Z. Fan, L. Xie, H. Zhang, W. Huang, T. Yu, Nitrogen and Sulfur Codoped Graphene: Multifunctional Electrode Materials for High-Performance Li-Ion Batteries and Oxygen Reduction Reaction, Adv. Mater. 26 (2014) 6186–6192, https://doi.org/10.1002/adma.201401427.

[66] S. Bag, B. Mondal, A.K. Das, C.R. Raj, Nitrogen and Sulfur Dual-Doped Reduced Graphene Oxide: Synergistic Effect of Dopants Towards Oxygen Reduction Reaction, Electrochim. Acta 163 (2015) 16–23, https://doi.org/10.1016/j.electacta.2015.02.130.

[67] W. Kiciński, M. Szala, M. Bystrzejewski, Sulfur-doped porous carbons: Synthesis and applications, Carbon N. Y. 68 (2014) 1–32, https://doi.org/10.1016/j.carbon.2013.11.004.

[68] M. Luis-Sunga, L. Regent, E. Pastor, G. García, Non-Precious Metal Graphene-Based Catalysts for Hydrogen Evolution Reaction, Electrochem 1 (2020) 75–86, https://doi.org/10.3390/electrochem1020008.

[69] D. Wu, T. Wang, L. Wang, D. Jia, Hydrothermal synthesis of nitrogen, sulfur co-doped graphene and its high performance in supercapacitor and oxygen reduction reaction, Micropor. Mesopor. Mater. 290 (2019), 109556, https://doi.org/10.1016/j.micromeso.2019.06.018.

[70] C. Long, D. Qi, T. Wei, J. Yan, L. Jiang, Z. Fan, Nitrogen-Doped Carbon Networks for High Energy Density Supercapacitors Derived from Polyaniline Coated Bacterial Cellulose, Adv. Funct. Mater. 24 (2014) 3953–3961, https://doi.org/10.1002/adfm.201304269.

[71] F. Zhang, X. Liu, M. Yang, X. Cao, X. Huang, Y. Tian, F. Zhang, H. Li, Novel S-doped ordered mesoporous carbon nanospheres toward advanced lithium metal anodes, Nano Energy 69 (2020), 104443, https://doi.org/10.1016/j.nanoen.2019.104443.

[72] D. Pech, M. Brunet, P. Taberna, P. Simon, N. Fabre, F. Mesnilgrente, V. Conédéra, H. Durou, Elaboration of a microstructured inkjet-printed carbon electrochemical capacitor, J. Power Sour. 195 (2010) 1266–1269, https://doi.org/10.1016/j.jpowsour.2009.08.085.

[73] W. Gao, N. Singh, L. Song, Z. Liu, A.L.M. Reddy, L. Ci, R. Vajtai, Q. Zhang, B. Wei, P.M. Ajayan, Direct laser writing of micro-supercapacitors on hydrated graphite oxide films, Nat. Nanotechnol. 6 (2011) 496–500, https://doi.org/10.1038/nnano.2011.110.

[74] D. Pech, M. Brunet, H. Durou, P. Huang, V. Mochalin, Y. Gogotsi, P.-L. Taberna, P. Simon, Ultrahigh-power micrometre-sized supercapacitors based on onion-like carbon, Nat. Nanotechnol. 5 (2010) 651–654, https://doi.org/10.1038/nnano.2010.162.

[75] Z. Liu, S. Liu, R. Dong, S. Yang, H. Lu, A. Narita, X. Feng, K. Müllen, High Power In-Plane Micro-Supercapacitors Based on Mesoporous Polyaniline Patterned Graphene, Small 13 (2017) 1603388, https://doi.org/10.1002/smll.201603388.

[76] J. Lin, C. Zhang, Z. Yan, Y. Zhu, Z. Peng, R.H. Hauge, D. Natelson, J.M. Tour, 3 - Dimensional Graphene Carbon Nanotube Carpet-Based Microsupercapacitors with High Electrochemical Performance, Nano Lett. 13 (2013) 72–78, https://doi.org/10.1021/nl3034976.

[77] M. Beidaghi, C. Wang, Micro-Supercapacitors Based on Interdigital Electrodes of Reduced Graphene Oxide and Carbon Nanotube Composites with Ultrahigh Power Handling Performance, Adv. Funct. Mater. 22 (2012) 4501–4510, https://doi.org/10.1002/adfm.201201292.

[78] J. Feng, X. Sun, C. Wu, L. Peng, C. Lin, S. Hu, J. Yang, Metallic Few-Layered VS 2 Ultrathin Nanosheets : High Two-Dimensional Conductivity for In-Plane Supercapacitors, J. Am. Chem. Soc. 133 (2011) 17832–17838, https://doi.org/10.1021/ja207176c.

[79] L. Cao, S. Yang, W. Gao, Z. Liu, Y. Gong, L. Ma, G. Shi, S. Lei, Y. Zhang, S. Zhang, R. Vajtai, Direct Laser-Patterned Micro-Supercapacitors from Paintable MoS 2 Films, Small 9 (2013) 2905–2910, https://doi.org/10.1002/smll.201203164.

[80] M.F. El-Kady, M. Ihns, M. Li, J.Y. Hwang, M.F. Mousavi, L. Chaney, A.T. Lech, R. B. Kaner, Engineering three-dimensional hybrid supercapacitors and microsupercapacitors for high-performance integrated energy storage, Proc. Natl. Acad. Sci. 112 (2015) 4233–4238, https://doi.org/10.1073/pnas.1420398112.